

Article

MoS₂/CdS Heterostructure for Enhanced Photoelectrochemical Performance under Visible Light

Guannan He ^{1,2,*} , Yimin Zhang ^{1,2,*} and Qinyu He ^{1,2}

¹ Guangdong Provincial Key Laboratory of Quantum Engineering and Quantum Materials, South China Normal University, Guangzhou 510006, Guangdong, China; gracylady@163.com

² Guangdong Engineering Technology Research Center of Efficient Green Energy and Environmental Protection Materials, Guangzhou 510006, Guangdong, China

* Correspondence: hegn@m.scnu.edu.cn (G.H.); amy.z@m.scnu.edu.cn (Y.Z.); Tel.: +86-20-39310066 (G.H.)

Received: 14 March 2019; Accepted: 22 April 2019; Published: 23 April 2019



Abstract: High-rate recombination of photogenerated electron and hole pairs will lead to low photocatalytic activity. Constructing heterostructure is a way to address this problem and thus increase the photoelectrochemical performance of the photocatalysts. In this article, molybdenum sulfide (MoS₂)/cadmium sulfide (CdS) nanocomposites were fabricated by a facile solvothermal method after sonication. The CdS nanoparticles immobilized on the MoS₂ sheet retained the original crystal structure and morphology. The composites exhibit higher photoelectrochemical properties compared with pure MoS₂ nanosheets or CdS powder. When the precursor concentration of CdS is 0.015 M, the MoS₂/CdS composites yield the highest photocurrent, which is enhanced nearly five times compared with pure CdS or MoS₂. The improved photoelectrochemical performance can be ascribed to the increase of light harvest, as well as to the heterostructure that decreases the recombination rate of the photogenerated electron and hole pairs.

Keywords: MoS₂ nanosheets; CdS nanoparticle; heterostructure; photocatalysis; photoelectrochemical properties

1. Introduction

Currently, the energy crisis and environmental pollution demand research on clean and renewable energy. Hydrogen as an environmental friendly and sustainable power source has been considered as a promising strategy to deal with the global energy problem. Photocatalytic hydrogen evolution from water splitting has attracted extensive interest. The semiconductors are used as catalysts to convert solar energy into hydrogen and, more importantly, the entire energy conversion process does not release a large amount of CO₂. Since TiO₂ was first employed on water splitting in 1972 [1], numerous semiconductor materials have been developed as photocatalysts for hydrogen production [2–5].

In the recent few years, two-dimensional (2D) materials have attracted wide attention because of their special optical and electronic properties, which make them suitable for applications in energy storage [6], transistors [7], photodetectors [8], electroluminescent devices [9], and especially catalysts [10–17]. Two-dimensional materials have many advantages over bulk materials, such as a lower surface energy barrier, more active sites, and a shorter carrier mobility distance [18]. Among them, molybdenum sulfide (MoS₂) has outstanding electronic, optical, and catalytic properties [7,19–21]. However, the photoelectrochemical properties of MoS₂ have been influenced by the high recombination rate of photogenerated carriers. Combining MoS₂ with other semiconductors can enhance light absorption and transfer efficiency of photogenerated electron-hole pairs. Furthermore, the internal

electrostatic field established in the heterostructure can separate the charges, thus decreasing the recombination rate of photogenerated carriers. Various MoS₂-based heterostructures like MoS₂/WS₂, MoS₂/ZnO, MoS₂/PbS, and MoS₂/C₃N₄ have been successfully fabricated as promising materials for photocatalysts [22–25]. Among these, cadmium sulfide (CdS) has recently received great interest owing to its direct suitable bandgap of 2.4 eV [26,27], which can be excited by the visible light of the solar spectrum to effectively generate charge carriers. Moreover, CdS has a suitable conduction band potential that is more negative than the reduction potential of H⁺/H₂ [28,29], making it a promising photocatalyst to be used in water splitting. Many studies have focused on CdS as a photocatalyst [30–32], but the high recombination rate of photogenerated carriers, lack of active sites, and photo-corrosion problems limit its application in photocatalytic hydrogen production [17].

In this article, we reported a 2D MoS₂/CdS nanocomposite heterostructure with CdS nanoparticles directly synthesized on MoS₂ nanosheets via a facile solvothermal method. The CdS nanoparticles immobilized on the MoS₂ sheets retained the original crystal structure and morphology. The size and the distribution of CdS particles were controlled by changing the concentration of the precursor. By combining with CdS, the light absorption spectrum of the nanocomposites was broadened and a significant enhancement on the photocurrent was achieved. We also used the Mott–Schottky curve to estimate the band position of CdS and MoS₂, which indicates the possible carrier activities under light irradiation.

2. Results and Discussion

The X-ray diffraction (XRD) patterns of as-prepared samples are displayed in Figure 1. The black curve is the XRD pattern of the pure MoS₂. The diffraction peaks located at around 14.4°, 32.7°, 33.5°, 35.7°, 39.6°, 44.2°, 49.8°, 58.4°, and 60.4°, which can be assigned to (002), (100), (101), (102), (103), (006), (105), (110), and (112) planes, respectively, of the hexagonal structure of MoS₂ crystalline (JCPDS file no. 87-2416). For the MoS₂/CdS nanocomposites, some new peaks were observed at 24.8°, 26.5°, 28.2°, 43.7°, 47.9°, and 51.9°, which can be assigned to (100), (002), (101), (110), (103), and (112) planes, respectively, of CdS (JCPDS file no. 70-2553). Further, these peaks were also shown in the pure CdS sample. No diffraction peaks of other impurities were detected, which indicates the high purity of the samples.

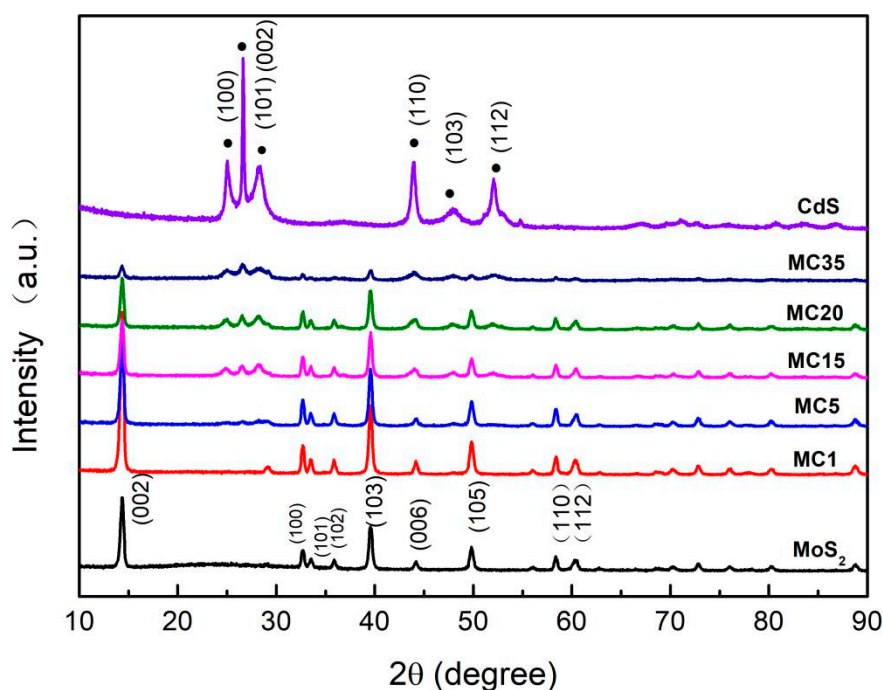


Figure 1. The X-ray diffraction (XRD) patterns of all the samples.

Figure 2a shows the scanning electron microscope (SEM) image of the as-obtained MoS₂, which exhibits a nanosheet-like shape with the thickness of 10–20 nm. The surface of the pure MoS₂ nanosheet is smooth, as shown in the high-resolution image (inset of Figure 2a). Figure 2b–f show the SEM images of MC1, MC5, MC15, MC20, and MC35, respectively. The combination with CdS has no influence on the sheet structure of MoS₂, but the surfaces of nanosheets become rough with the addition of CdS. As shown in the high-resolution images (insets of Figure 2b–f), CdS nanoparticles scatter on the surfaces of the pristine MoS₂ nanosheets. When the precursor concentration of Cd²⁺ is low, the size of CdS nanoparticles is small and the distribution of the nanoparticles is uniform, as shown in samples MC1, MC5, and MC15. However, as the concentration of precursor solution increases, the size of CdS nanoparticles increases. Even large agglomerates of CdS particles were observed in samples MC20 and MC35, as shown in the insets of Figure 2e,f.

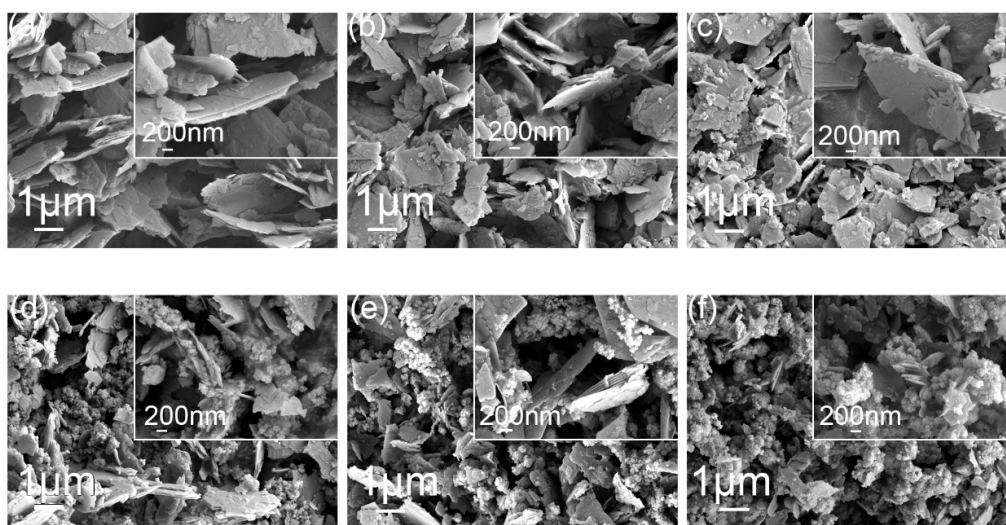


Figure 2. Scanning electron microscope (SEM) images of (a) molybdenum sulfide (MoS₂) nanosheets; (b) MC1; (c) MC5; (d) MC15; (e) MC20; (f) MC35.

Figure 3a shows the transmission electron microscopy (TEM) image of MC15. The sheet structure of MoS₂, as well as the uniform size and distribution of CdS nanoparticles, are clearly exhibited, which corresponds with the SEM result. The high-resolution TEM (HRTEM) image of MC15 sample is shown in Figure 3b. Apparently, the fringe with the lattice spacing of 0.27 nm corresponds to (100) plane of MoS₂, and the other fringe with the lattice spacing of 0.36 nm corresponds to the (100) plane of CdS. The CdS lattices are well contacted with that of MoS₂, which indicates that an interfacial heterostructure formed between CdS and MoS₂. The intimate heterostructure can promote the charge transfer and thus reduce the recombinations of photogenerated electron and hole pairs.

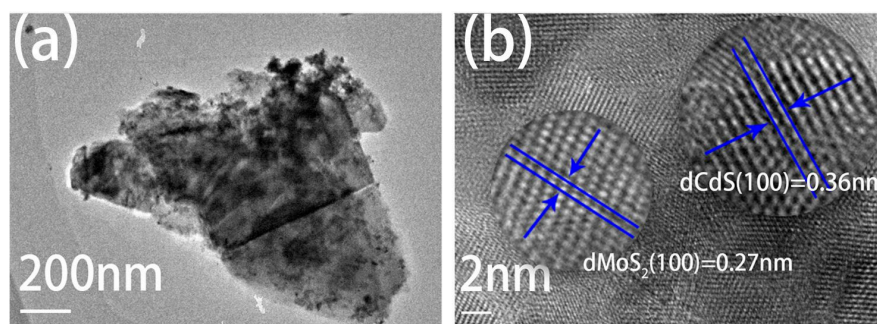


Figure 3. (a) Transmission electron microscopy (TEM) image of MC15; (b) high-resolution TEM (HRTEM) image of MC15.

The X-ray photoelectron spectroscopy (XPS) analysis was performed to study the surface composition and chemical state of sample MC15. The peak positions are calibrated with C 1s at 285.3 eV. The XPS spectra (Figure 4a) show that the elements including Mo, Cd, and S are contained in sample MC15. This result confirms that MoS₂ and CdS coexist in the sample. Figure 4b–d show the high-resolution spectra of Cd 3d, Mo 3d, S 2s, and S 2p. Figure 4b displays two peaks located at around 405.8 eV and 412.5 eV, which are assigned to the binding energy of Cd 3d_{5/2} and Cd 3d_{3/2}, respectively. In Figure 4c, the spectra can be fitted into three peaks. Two of them located at 232.5 eV and 229.4 eV correspond to Mo⁴⁺ 3d_{3/2} and Mo⁴⁺ 3d_{5/2}, respectively. The peak at 226.6 eV is assigned to the binding energy of S 2s. Besides, Figure 4d is the high resolution XPS spectra of S 2p, which can be divided into two peaks at around 162.3 eV and 163.3 eV corresponding to the binding energy of S 2p_{3/2} and S 2p_{1/2}, respectively.

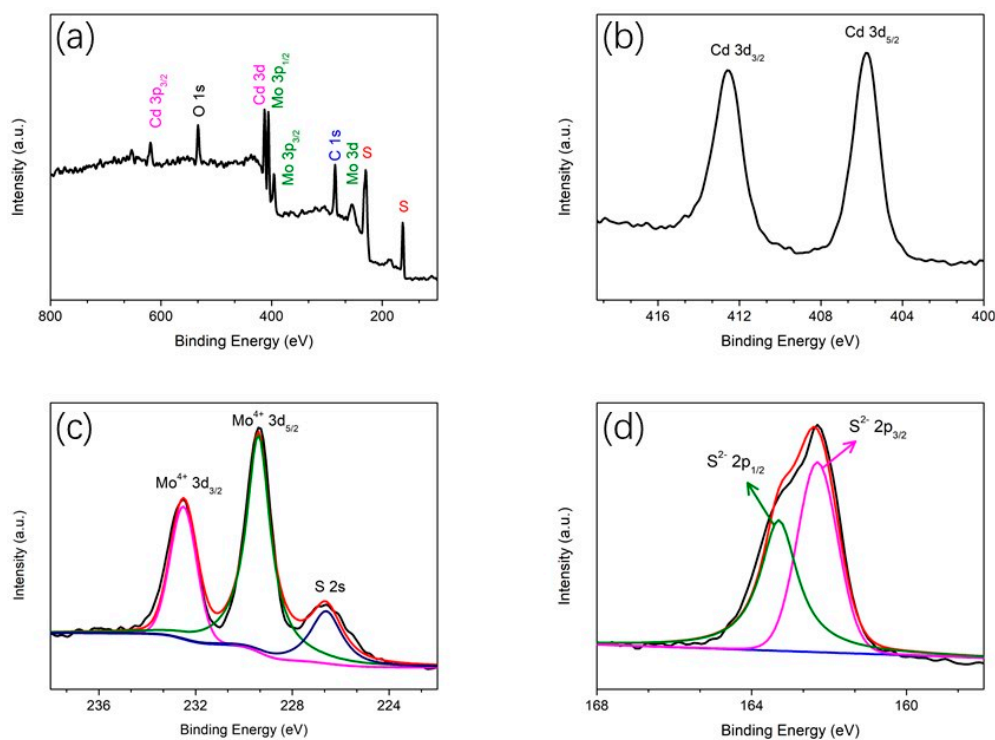


Figure 4. X-ray photoelectron spectroscopy (XPS) spectra of MC15: (a) survey spectra; (b) Cd 3d spectra; (c) Mo 3d and S 2s spectra; (d) S 2p spectra.

The UV-vis absorption spectra of all the samples are shown in Figure 5a. The absorption peaks of pure MoS₂ nanosheets appear at the wavelengths ranging from 600 nm to 700 nm, which is in accordance with the previous report by H. J. Kim, et al. [33]. Compared with the pure MoS₂, the MoS₂/CdS nanocomposites also exhibit similar spectra from 600 nm to 800 nm wavelengths. However, with the increasing amount of CdS, the samples display a remarkable enhancement over the wavelengths ranging from 300 nm to 500 nm. The results indicate that the combination with CdS can extend the absorption spectra. The band gaps of MoS₂ and CdS are estimated to be 1.58 eV and 2.45 eV, respectively, using Tauc's plot, as shown in Figure 5b, which is in agreement with the previous reports [10,29].

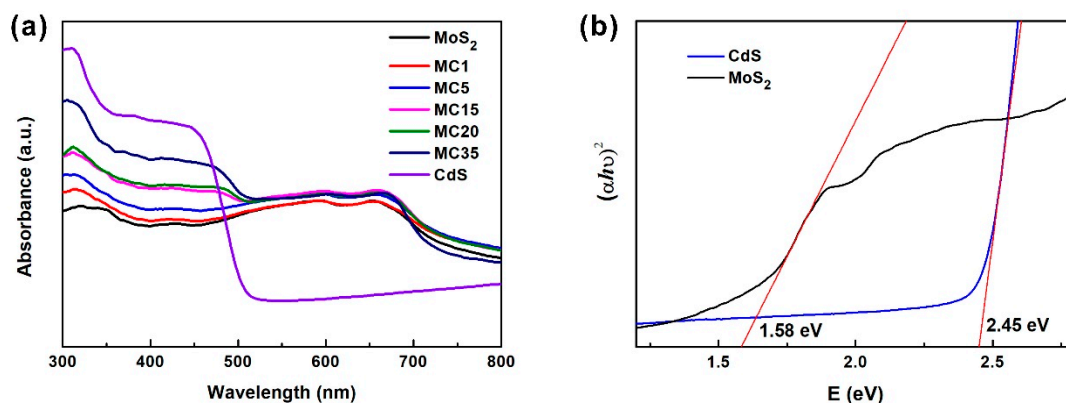


Figure 5. (a) UV-vis absorption spectra; (b) band gaps of MoS₂ and CdS estimated by $(\alpha h\nu)^2$ vs. photon energy curve.

To further study the photogenerated charge carrier transfer properties, transient photocurrent responses were measured by several on–off intermittent visible light irradiation cycles, and the differences between I_{on} and I_{off} (ΔI s) are shown in Figure 6a. The ΔI s of the MoS₂/CdS composites are higher compared with those of the pure MoS₂ nanosheets and the pure CdS nanoparticles. Two reasons may contribute to the enhancement of the photocurrent. Firstly, the broadened absorption spectra of nanocomposites indicate that more photons have been absorbed by the photocatalysts and thus more electron and hole pairs may be generated. Secondly, the MoS₂/CdS heterojunction structure can efficiently separate the photogenerated electron and hole pairs, and finally reduce the recombination rate of photogenerated carriers. MC15 exhibits the highest ΔI , which is close to five times that of the pristine MoS₂. The ΔI decrease of the sample MC20 and MC35 may be the result of the large size and agglomeration of CdS nanoparticles, which can reduce the contact area between MoS₂ nanosheets and CdS nanoparticles and affect the separation rate of photogenerated carriers. This result is consistent with SEM images (Figure 2e,f), which show CdS nanoparticles with larger size and agglomerate status in these two samples. Moreover, compared with pure CdS and pure MoS₂, the composites exhibit obvious transients when switching from light on to light off. This phenomenon may be because of the heterojunction formed between CdS and MoS₂ in the composites. Because of the capacity effect of the heterojunction, when the light is turned on, the capacitor is charged slowly, so a slow current increase can be observed. Also, when switching from light on to light off, the capacitor is slowly discharged, which results in the long transient. Besides, there is a decreasing trend of photocurrent, especially in the sample with a high photocurrent. This may be because of the decrease of the diffusion rate of the sacrificial agents. The concentration of sacrificial agents around the catalysts is high at the beginning of the measurement, so the photocurrent is larger. Meanwhile, the consumption of the sacrificial agents is higher at a large current. As the reaction continues, the concentration of the sacrificial agents decreases, which induces the decrease of concentration gradient between the surface of the catalysts and the surrounding solution. Thus, the diffusion rate of the sacrificial agents decreases, which results in the decreasing trend of the photocurrent. This phenomenon is remarkable at a high current.

The linear sweep voltammetry (LSV) measurement was chosen to evaluate the hydrogen evolution reaction (HER) performance of nanocomposites by comparing with pure MoS₂ and pure CdS. The measurements were performed using three-electrode system in a mixed electrolyte with 0.25 M Na₂S and 0.35 M Na₂SO₃. As shown in Figure 6b, pure MoS₂ and pure CdS display poor photocatalytic activities with high onset potentials about -0.5 V versus reversible hydrogen electrode (vs. RHE). The MoS₂/CdS nanocomposites exhibit varying degrees of improvement on catalytic performance, with onset potentials ranging from -0.40 V to -0.25 V (vs. RHE). MC15 shows superior catalytic activities with the lowest onset potential of approximately -0.25 V, and the current density at -0.5 V is nearly 10 times that of pure MoS₂. Moreover, by comparing with the data obtained

without light illumination, sample MC15 exhibits a large positive shift on onset potential, indicating its high photoresponsivity.

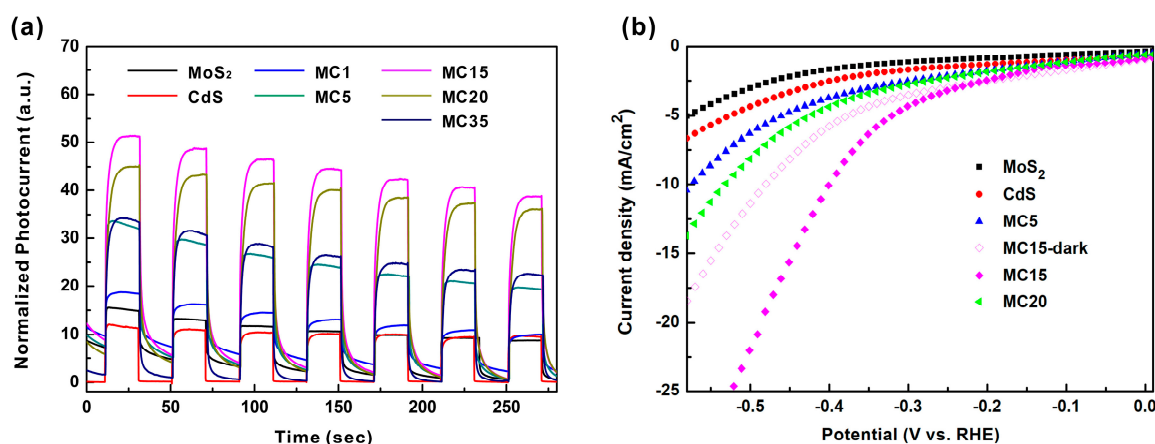


Figure 6. (a) Photocurrent responses of MoS₂, CdS, and MoS₂/CdS nanocomposites; (b) polarization curves of MoS₂, CdS, MC5, MC15, and MC20.

Electrochemical impedance spectroscopy (EIS) is a useful way to characterize the interfacial charge transfer effects of the prepared samples. Figure 7 shows the EIS Nyquist plots of pure CdS and MoS₂/CdS nanocomposites, and the curves are fitted by ZSimpwin software using an equivalent circuit shown in the inset of Figure 7. In the equivalent circuit, R_s is the resistance of the solution, CPE is the equivalent element of double electric layer, and R_{ct} is the charge transfer resistance. As reported, the arc radius of the EIS spectrum reflects the R_{ct} on the interface [34]. So, Table 1 lists the corresponding R_{ct} simulated by ZSimpwin. The pure CdS has the largest R_{ct} , indicating its highest charge transfer resistance and low surface electron mobility. This may lead to the low separation rate of photogenerated electrons and holes. By combining with MoS₂, the composites have smaller arc radii and lower R_{ct} compared with pure CdS, which indicates that the composites have smaller surface resistance and faster surface electron mobility than pure CdS. The R_{ct} value of MC35 is much higher than that of MC1, MC5, MC15, and MC20, which indicate that a high CdS/MoS₂ molar ratio causes low separation and mobility of photogenerated carriers, and thus influences the photoelectric performance.

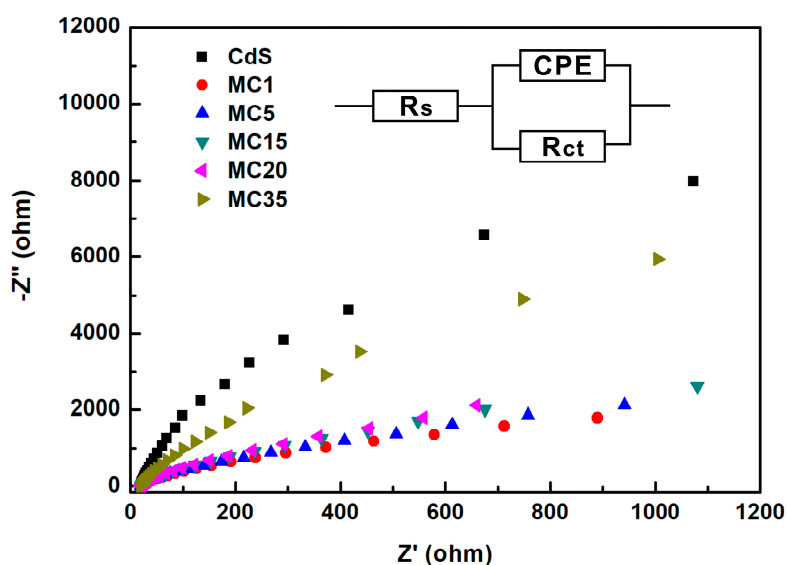


Figure 7. Electrochemical impedance spectroscopy (EIS) Nyquist plots of CdS and MoS₂/CdS nanocomposites. CPE— equivalent element of double electric layer.

Table 1. Charge transfer resistances (R_{ct}) of cadmium sulfide (CdS) and molybdenum sulfide (MoS_2)/CdS nanocomposites.

Sample	CdS	MC1	MC5	MC15	MC20	MC35
R_{ct}/Ω	6.765×10^4	6903	7389	8032	1.183×10^4	5.108×10^4

The Mott–Schottky plots can be used to investigate the semiconductor type and the flat band potential (E_{FB}) of the materials [10,29]. The positive slopes of the plots indicate that MoS_2 and CdS are both n-type semiconductors. Furthermore, the intercept of the x-axis indicates the E_{FB} potential of the semiconductor. As displayed in Figure 8, the E_{FB} positions of MoS_2 and CdS are estimated to be -0.11 V and -0.60 V (vs. RHE), respectively. The gap between E_{FB} and the bottom of the conduction band (CB) is usually negligible in n-type semiconductors [35]. Thus, the CB potential of MoS_2 is estimated to be -0.11 V (vs. RHE) or -0.51 V versus normal hydrogen electrode (vs. NHE). The CB potential of CdS is around -0.60 V (vs. RHE) or -1.00 V (vs. NHE). The E_g values of MoS_2 and CdS are 1.58 eV and 2.45 eV, respectively, as shown in Figure 5b. Therefore, the valence band (VB) potentials of MoS_2 and CdS are 1.47 V and 1.85 V (vs. RHE) or 1.07 V and 1.45 V (vs. NHE), respectively. The band potentials of MoS_2 and CdS are illustrated in Figure 9.

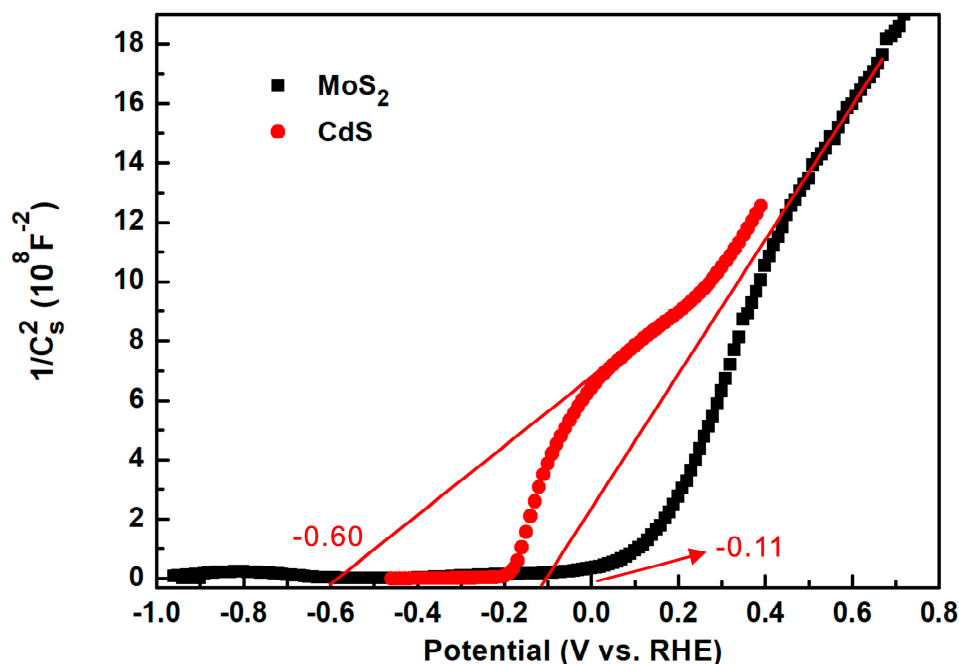
**Figure 8.** Mott–Schottky curves of pure MoS_2 and CdS. RHE—reversible hydrogen electrode.

Figure 9 illuminates the mechanism of the MoS_2/CdS photocatalyst on the enhanced photoelectrochemical performance. The combination with CdS firstly extends the absorption spectra. Furthermore, the CdS nanoparticles distribute uniformly on the surface of MoS_2 nanosheets to form intimate heterostructures, which can promote the charge transfer and the separation efficiency of photogenerated electron and hole pairs. Under visible light illumination, the electrons in the VB of CdS and MoS_2 can be excited to the CB to create photogenerated electron-hole pairs. Under the thermodynamic driving force, the electrons from the excited CdS firstly transfer to MoS_2 , and then the electrons from the CB of both MoS_2 and CdS will shift through the fluorine-doped tin oxide (FTO) and the external circuit, and in the end will reach the Pt counter electrode for water splitting. The effective charge separation contributes to the enhanced photoelectrochemical properties, as shown in sample MC15. The contact interface between CdS and MoS_2 plays an important role on the photoelectrochemical activities of the MoS_2/CdS photocatalyst. A certain amount of CdS should be

contained in order to guarantee the activity of the photocatalyst and establish the heterostructure with MoS₂. However, excessive CdS will lead to oversized particles and even agglomerates, which may decrease the contact area between CdS and MoS₂, resulting in low charge carriers separation and transfer rate, as shown in sample MC35. Meanwhile, Na₂S in aqueous solution releases hydroxide (OH⁻) ions and hydrogen sulfide (HS⁻) ions. The holes accumulated on the VB of CdS and MoS₂ will be consumed by reacting with HS⁻, which can inhibit the corrosion of CdS and MoS₂. Therefore, the heterostructure can efficiently separate the photogenerated electron and hole pairs and improve the photoelectrochemical performance of the photocatalysts. The relative reactions can be summarized as follows [36,37]:

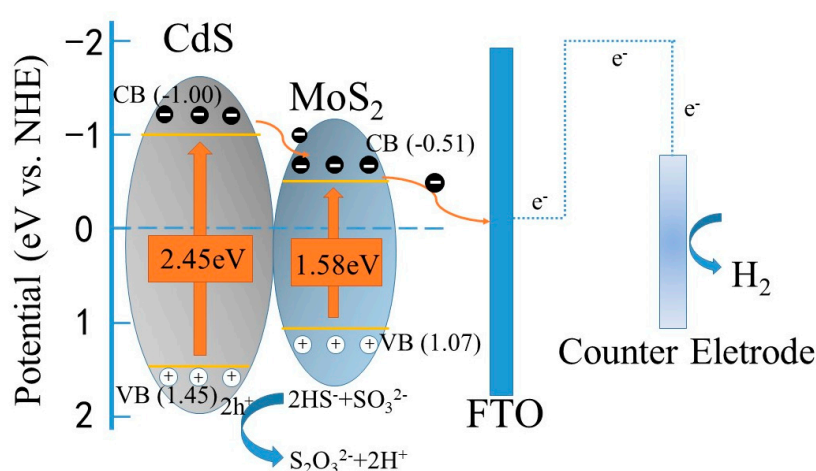
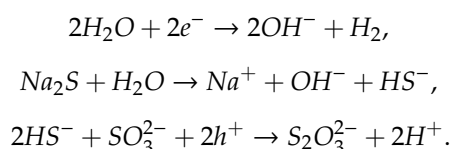


Figure 9. Schematic of the MoS₂ sheets/CdS nanoparticles heterojunction photocatalytic system. FTO—fluorine-doped tin oxide; NHE—normal hydrogen electrode; CB—conduction band; VB—valence band.

3. Experimental Section

3.1. Materials

Bulk molybdenum sulfide (MoS₂) was purchased from Aladdin (Shanghai, China). Cadmium nitrate tetrahydrate (Cd(NO₃)₄·4H₂O) and thiourea (NH₂CSNH₂) were purchased from Macklin (Shanghai, China), and N,N-Dimethyl formamide (DMF) was purchased from Zhiyuan Co., Ltd. (Tianjin, China). All the chemicals are analytical pure (AR) and used without further purification. Fluorine-doped tin oxide (FTO) glass was purchased from Jinge-solar Energy Technology Co., Ltd. (Wuhan, China).

3.2. Preparation of MoS₂ Nanosheets

MoS₂ nanosheets were exfoliated from bulk MoS₂ crystals by the ultrasonic method. A total of 0.1 g MoS₂ power was added into the beaker with 100 mL DMF solution. The mixture was stirred for 10 min at room temperature, and then kept sonicated for 10 h with an ultrasonic power of 200 W. Subsequently, the top two-thirds of the dispersion was extracted and stirred for 12 h at room temperature. The resulting solution was collected and used to form MoS₂/CdS nanocomposites.

3.3. Synthesis of MoS₂/CdS Nanocomposites

A solvothermal method was employed to synthesize MoS₂/CdS nanocomposites. Typically, Cd(NO₃)₂·4H₂O and NH₂CSNH₂ in a 1:2 M ratio were dispersed in 15 mL DMF and then stirred for 10 min until a uniform and transparent solution was formed prior to being mixed with 60 mL MoS₂ flakes solution in a 100 mL Teflon-lined stainless steel autoclave. Next, the autoclave was heated at 180 °C for 2 h and then cooled down to room temperature. The resulting precipitates were collected by centrifugation and washed with deionized water and dried at 60 °C in air. The obtained yellow-green powder was MoS₂/CdS nanocomposites. The mixed solution with Cd(NO₃)₂·4H₂O concentration of 0.001, 0.005, 0.015, 0.02, and 0.035 mol/L was labeled as MC1, MC5, MC15, MC20, and MC35, respectively.

3.4. Synthesis of Pure CdS Nanoparticles

Cd(NO₃)₂·4H₂O (0.015 mol/L) and thiourea in a 1:2 M ratio were dispersed in 100 mL DMF in a beaker, and stirred for 10 min until the solution become transparent, after which 75 mL of the solution was moved into a 100 mL autoclave and heated at 180 °C for 2 h, and then cooled down to room temperature. The resulting yellow CdS power was collected by centrifugation and washed with deionized water and dried at 60 °C in air.

3.5. Characterization

The crystalline structures of all the samples were analyzed by an X-ray diffractometer (XRD) (BRUKER D8 ADVANCE, BRUKER, Billerica, MA, USA) and measured within 2θ range from 10° to 90°. The morphologies and structures of the photocatalysts were characterized via scanning electron microscopy (SEM) (ZEISS Gemini 500, Carl Zeiss Company, Oberkochen, Germany) and transmission electron microscopy (TEM) (JEM-2100HR, Japan Electron Optics Laboratory, Tokyo, Japan). The chemical states of the elements were analyzed using X-ray photoelectron spectroscopy (XPS) (PHI X-tool, ULVAC-PHI Inc., Kanagawa, Japan) with Al Kα as excitation source. The UV-vis absorption spectra of the samples were characterized by a UV-vis spectrophotometer (UV-Vis-DRS, SHIMADZU, Kyoto, Japan).

3.6. Photoelectrochemical and Electrochemical Performance Measurements

The photoelectrochemical measurements of the samples were analyzed on an electrochemical analyzer (CHI660D, Shanghai Chenhua Instrument Company, Shanghai, China) using a standard three-electrode system. Pt was used as counter electrode and Ag/AgCl (saturated KCl) was used as reference electrode. The work electrode was prepared by dispensing approximately 10 mg of the synthesized powder into DMF solution, and then dripping onto the FTO wafer with a fixed size of 1.5 × 1.5 cm². The obtained electrodes were dried in an oven at 80 °C for 2 h. A solution containing 0.35 M Na₂SO₃ and 0.25 M Na₂S was used as electrolyte, and the pH value was 12. The photocurrent response measurement was performed at the potential condition of 0.5 V versus Ag/AgCl (saturated KCl). The hydrogen evolution reaction (HER) activity of the sample was characterized by linear sweep voltammetry (LSV) with a scanning rate of 10 mV/s, from −0.6 V to 0 V (vs. RHE). Xe lamp was used as the light source with the illumination intensity of 100 mW/cm².

The electrochemical impedance spectroscopy (EIS) and the Mott–Schottky test were performed on an electrochemical analyzer (CHI660D, Shanghai Chenhua Instrument Company, Shanghai, China) using a standard three-electrode system. The EIS plots were measured at 0 V versus Ag/AgCl (saturated KCl) from 10⁴ to 10^{−1} Hz, with an alternating current (AC) voltage magnitude of 5 mV. The Mott–Schottky test was performed from −1.0 V to 0.8 V (vs. RHE) with a frequency of 10 Hz. 0.5 M Na₂SO₄ aqueous solution was chosen as the electrolyte for EIS and Mott–Schottky measurements. The pH value of the electrolyte was 6.7. The potentials appeared in this paper were all converted to the reversible hydrogen electrode (RHE) as Nernst equation [29]: $E_{RHE} = 0.0591pH + E_{Ag/AgCl} + 0.197$.

4. Conclusions

MoS₂/CdS heterostructure photocatalysts were fabricated using a simple solvothermal process after sonication. The characterization suggests that the CdS nanoparticles immobilized on the MoS₂ sheet retained the original crystal structure and morphology. The introduction of CdS not only extends the light absorption spectra, but also promotes the charge transfer and the separation efficiency of photogenerated charge carriers via heterostructure, and thus significantly enhances the photoelectrochemical performance of photocatalysts. The MC15 shows the highest photocatalytic property, with the photocurrent density being nearly five times that of the pristine MoS₂. This article provides an effective way to improve the photoelectrochemical properties of photocatalysts and we believe this material has promising applications in photocatalytic hydrogen evolution with high efficiency and low cost.

Author Contributions: Methodology, G.H. and Y.Z.; Validation, G.H.; Formal analysis, Y.Z.; Data curation, G.H.; Writing—Original Draft preparation, G.H.; Writing—Review and Editing, Y.Z. and Q.H.

Funding: The work was financially supported by The Provincial Natural Science Foundation of Guangdong Province, China (No. 2017A030310064); and The National Natural Science Foundation of China (No. 61307080, No. 61404052, No. 51372092, No.51672090).

Conflicts of Interest: The authors declare no conflict of interest.

References

1. Fujishima, A.; Honda, K. Electrochemical photolysis of water at a semiconductor electrode. *Nature* **1972**, *238*, 37–38. [[CrossRef](#)]
2. Han, J.S.; Dai, F.X.; Liu, Y.; Zhao, R.Y.; Wang, L.; Feng, S.H. Synthesis of CdSe/SrTiO₃ nanocomposites with enhanced photocatalytic hydrogen production activity. *Appl. Surf. Sci.* **2019**, *467*, 1033–1039. [[CrossRef](#)]
3. Zhu, Y.W.; Wang, L.L.; Liu, Y.T.; Shao, L.H.; Xia, X.N. In-situ hydrogenation engineering of ZnIn₂S₄ for promoted visible-light water splitting. *Appl. Catal. B-Environ.* **2019**, *241*, 483–490. [[CrossRef](#)]
4. Bian, T.; Shang, L.; Yu, H.J.; Perez, M.T.; Wu, L.Z.; Tung, C.H.; Nie, Z.H.; Tang, Z.Y.; Zhang, T.R. Spontaneous organization of inorganic nanoparticles into nanovesicles triggered by UV light. *Advanced Mater.* **2014**, *26*, 5613–5618. [[CrossRef](#)] [[PubMed](#)]
5. Ruan, D.M.; Kim, S.; Fujitsuka, M.; Majima, T. Defects rich g-C₃N₄ with mesoporous structure for efficient photocatalytic H₂ production under visible light irradiation. *Appl. Catal. B-Environ.* **2018**, *238*, 638–646. [[CrossRef](#)]
6. Yang, Y.; Luo, M.C.; Xing, Y.; Wang, S.T.; Zhang, W.Y.; Lv, F.; Li, Y.J.; Zhang, Y.L.; Wang, W.; Guo, S.J. A universal strategy for intimately coupled carbon nanosheets/MoM nanocrystals (M = P, S, C, and O) hierarchical hollow nanospheres for hydrogen evolution catalysis and sodium-ion storage. *Adv. Mater.* **2018**, *30*, 1706085. [[CrossRef](#)]
7. Wang, Q.H.; Kalantar-Zadeh, K.; Kis, A.; Coleman, J.N.; Strano, M.S. Electronics and optoelectronics of two-dimensional transition metal dichalcogenides. *Nat. Nanotechnol.* **2012**, *7*, 699–712. [[CrossRef](#)]
8. Song, X.F.; Hu, J.L.; Zeng, H.B. Two-dimensional semiconductors: Recent progress and future perspectives. *J. Mater. Chem. C* **2013**, *1*, 2952–2969. [[CrossRef](#)]
9. Xie, J.F.; Zhang, H.; Li, S.; Wang, R.X.; Sun, X.; Zhou, M.; Zhou, J.F.; Lou, X.W.; Xie, Y. Defect-rich MoS₂ ultrathin nanosheets with additional active edge sites for enhanced electrocatalytic hydrogen evolution. *Adv. Mater.* **2013**, *25*, 5807–5813. [[CrossRef](#)] [[PubMed](#)]
10. Anpo, M.; Takeuchi, M. The design and development of highly reactive titanium oxide photocatalysts operating under visible light irradiation. *J. Catal.* **2003**, *216*, 505–516. [[CrossRef](#)]
11. Asahi, R.; Morikawa, T.; Ohwaki, T.; Aoki, K.; Taga, Y. Visible-light photocatalysis in nitrogen-doped titanium oxides. *Science* **2001**, *293*, 269–271. [[CrossRef](#)]
12. Bu, Y.Y.; Chen, Z.Y.; Sun, C.J. Highly efficient Z-Scheme Ag₃PO₄/Ag/WO_{3-x} photocatalyst for its enhanced photocatalytic performance. *Appl. Catal. B-Environ.* **2015**, *179*, 363–371. [[CrossRef](#)]
13. Chang, K.; Mei, Z.W.; Wang, T.; Kang, Q.; Ouyang, S.X.; Ye, J.H. MoS₂/Graphene cocatalyst for efficient photocatalytic H₂ evolution under visible light irradiation. *ACS Nano* **2014**, *8*, 7078–7087. [[CrossRef](#)] [[PubMed](#)]

14. Chen, G.P.; Li, D.M.; Li, F.; Fan, Y.Z.; Zhao, H.F.; Luo, Y.H.; Yu, R.C.; Meng, Q.B. Ball-milling combined calcination synthesis of MoS₂/CdS photocatalysts for high photocatalytic H₂ evolution activity under visible light irradiation. *Appl. Catal. A-Gen.* **2012**, *443*, 138–144. [[CrossRef](#)]
15. Feng, C.; Chen, Z.; Hou, J.; Li, J.; Li, X.; Xu, L.; Sun, M.; Zeng, R. Effectively enhanced photocatalytic hydrogen production performance of one-pot synthesized MoS₂ clusters/CdS nanorod heterojunction material under visible light. *Chem. Eng. J.* **2018**, *345*, 404–413. [[CrossRef](#)]
16. Habba, Y.G.; Capochichi-Gnambodoe, M.; Leprince-Wang, Y. Enhanced photocatalytic activity of iron-doped ZnO nanowires for water purification. *Appl. Sci.* **2017**, *7*, 1185. [[CrossRef](#)]
17. Kudo, A.; Miseki, Y. Heterogeneous photocatalyst materials for water splitting. *Chem. Soc. Rev.* **2009**, *38*, 253–278. [[CrossRef](#)]
18. Li, X.L.; Wang, X.J.; Zhu, J.Y.; Li, Y.P.; Zhao, J.; Li, F.T. Fabrication of two-dimensional Ni₂P/ZnIn₂S₄ heterostructures for enhanced photocatalytic hydrogen evolution. *Chem. Eng. J.* **2018**, *353*, 15–24. [[CrossRef](#)]
19. Radisavljevic, B.; Radenovic, A.; Brivio, J.; Giacometti, V.; Kis, A. Single-layer MoS₂ transistors. *Nat. Nanotechnol.* **2011**, *6*, 147–150. [[CrossRef](#)]
20. Splendiani, A.; Sun, L.; Zhang, Y.B.; Li, T.S.; Kim, J.; Chim, C.Y.; Galli, G.; Wang, F. Emerging Photoluminescence in Monolayer MoS₂. *Nano Lett.* **2010**, *10*, 1271–1275. [[CrossRef](#)]
21. Parzinger, E.; Miller, B.; Blaschke, B.; Garrido, J.A.; Ager, J.W.; Holleitner, A.; Wurstbauer, U. Photocatalytic stability of single- and few-layer MoS₂. *ACS Nano* **2015**, *9*, 11302–11309. [[CrossRef](#)]
22. Xu, S.J.; Li, D.; Wu, P.Y. One-pot, facile, and versatile synthesis of monolayer MoS₂/WS₂ quantum dots as bioimaging probes and efficient electrocatalysts for hydrogen evolution reaction. *Adv. Funct. Mater.* **2015**, *25*, 1127–1136. [[CrossRef](#)]
23. Tan, Y.H.; Yu, K.; Li, J.Z.; Fu, H.; Zhu, Z.Q. MoS₂@ZnO nano-heterojunctions with enhanced photocatalysis and field emission properties. *J. Appl. Phys.* **2014**, *116*, 064305. [[CrossRef](#)]
24. Li, M.; Ruan, H.R.; Yuan, X.Q.; Chen, Y.S.; Wang, X.D.; Liu, Y.P.; Lu, Z.H.; Hai, J.F. Construction of 2D MoS₂/PbS heterojunction nanocomposites with enhanced photoelectric property. *Mater. Lett.* **2018**, *212*, 82–85. [[CrossRef](#)]
25. Fageria, P.; Sudharshan, K.Y.; Nazir, R.; Basu, M.; Pande, S. Decoration of MoS₂ on g-C₃N₄ surface for efficient hydrogen evolution reaction. *Electrochim. Acta* **2017**, *258*, 1273–1283. [[CrossRef](#)]
26. Yang, J.H.; Wang, D.G.; Han, H.X.; Li, C. Roles of cocatalysts in photocatalysis and photoelectrocatalysis. *Accounts Chem. Res.* **2013**, *46*, 1900–1909. [[CrossRef](#)]
27. Yin, Y.X.; Jin, Z.G.; Hou, F. Enhanced solar water-splitting efficiency using core/sheath heterostructure CdS/TiO₂ nanotube arrays. *Nanotechnology* **2007**, *18*, 495608. [[CrossRef](#)] [[PubMed](#)]
28. Kumar, D.P.; Hong, S.; Reddy, D.A.; Kim, T.K. Ultrathin MoS₂ layers anchored exfoliated reduced graphene oxide nanosheet hybrid as a highly efficient cocatalyst for CdS nanorods towards enhanced photocatalytic hydrogen production. *Appl. Catal. B Environ.* **2017**, *212*, 7–14. [[CrossRef](#)]
29. Zheng, Z.X.; Qiao, Y.; Cai, Y.H.; He, Y.N.; Tang, Y.M.; Li, L.S. MoS₂ decorated CdS hybrid heterojunction for enhanced photoelectrocatalytic performance under visible light irradiation. *J. Colloid Interface Sci.* **2019**, *533*, 561–568. [[CrossRef](#)]
30. Bie, C.B.; Fu, J.W.; Cheng, B.; Zhang, L.Y. Ultrathin CdS nanosheets with tunable thickness and efficient photocatalytic hydrogen generation. *Appl. Surf. Sci.* **2018**, *462*, 606–614. [[CrossRef](#)]
31. Liu, Z.M.; Liu, G.L.; Hong, X.L. Influence of surface defects and palladium deposition on the activity of CdS nanocrystals for photocatalytic hydrogen production. *Acta Phys.-Chim. Sin.* **2019**, *35*, 215–222.
32. Zhao, Y.; Fang, Z.B.; Feng, W.H.; Wang, K.Q.; Huang, X.Y.; Liu, P. Hydrogen production from pure water via piezoelectric-assisted visible-light photocatalysis of CdS nanorod arrays. *ChemCatChem* **2018**, *10*, 3397–3401. [[CrossRef](#)]
33. Kim, H.J.; Song, Y.W.; Namgung, S.D.; Song, M.K.; Yang, S.; Kwon, J.Y. Optical properties of the crumpled pattern of selectively layered MoS₂. *Opt. Lett.* **2018**, *43*, 4590–4593. [[CrossRef](#)] [[PubMed](#)]
34. Zhang, Q.; Hu, S.Z.; Fan, Z.P.; Liu, D.S.; Zhao, Y.F.; Ma, H.F.; Li, F.Y. Preparation of g-C₃N₄/ZnMoCdS hybrid heterojunction catalyst with outstanding nitrogen photofixation performance under visible light via hydrothermal post-treatment. *Dalton Trans.* **2016**, *45*, 3497–3505. [[CrossRef](#)]
35. Premkumar, J. Development of super-hydrophilicity on nitrogen-doped TiO₂ thin film surface by photoelectrochemical method under visible light. *Chem. Mater.* **2004**, *16*, 3980–3981. [[CrossRef](#)]

36. Liu, Z.Q.; Cao, X.H.; Wang, B.; Xia, M.; Lin, S.; Guo, Z.H.; Zhang, X.M.; Gao, S.Y. Coupling thermoelectricity and electrocatalysis for hydrogen production via PbTe-PbS/TiO₂ heterojunction. *J. Power Sources* **2017**, *342*, 452–459. [[CrossRef](#)]
37. Bai, J.; Li, J.H.; Liu, Y.B.; Zhou, B.X.; Cai, W.M. A new glass substrate photoelectrocatalytic electrode for efficient visible-light hydrogen production: CdS sensitized TiO₂ nanotube arrays. *Appl. Catal. B-Environ.* **2010**, *95*, 408–413. [[CrossRef](#)]



© 2019 by the authors. Licensee MDPI, Basel, Switzerland. This article is an open access article distributed under the terms and conditions of the Creative Commons Attribution (CC BY) license (<http://creativecommons.org/licenses/by/4.0/>).